ELSEVIER

Direct numerical simulations of turbulent forced convection between counter-rotating disks

Roger W. Hill [a], Kenneth S. Ball [b,*]

[a] *Department of Mechanical and Aerospace Engineering, University of Missouri-Columbia, Columbia, MO 65211, USA*
[b] *Department of Mechanical Engineering, The University of Texas at Austin, Austin, TX 78712, USA*

Abstract

A Fourier–Chebyshev collocation spectral method is used to simulate the three dimensional unsteady flow inside a cylindrical annular enclosure comprised of two counter-rotating disks and sidewalls. Each disk is taken to be isothermal, with an imposed temperature difference between them, and the sidewalls are adiabatic. Buoyancy forces are neglected. A shallow annulus with aspect ratio, $h/r_o = 0.06$, and radius ratio, $r_i/r_o = 0.13$, is considered (where $2h$ is the distance between the disks and r_i and r_o are the inner and outer disk radii, respectively). One disk is rotating at the maximum speed and the other disk is rotating in the opposite direction. Results are obtained over a range of Re including the transition from laminar flow, for cases with both disks rotating at the same speed, $\Gamma = -1.0$, with one disk rotating more slowly than the other, $\Gamma = -0.4$, and with one stationary disk, $\Gamma = 0$ (where Γ is the disk angular velocity ratio). The heat transfer rates between the disks are also obtained, showing the effects of transition to turbulence. The three-dimensional nature of the flows is characterized, and mean and RMS turbulence quantities are presented. © 1999 Elsevier Science Inc. All rights reserved.

Keywords: Direct numerical simulations; Transition; Turbulence; Counter-rotating disks; Spectral methods

Notation

$2h$	disk spacing
Nu	Nusselt number
p	dimensional pressure
P	dimensionless pressure
Pe	Peclet number
Pr	Prandtl number
r, z	dimensional radial and axial coordinates, respectively
R, Z	dimensionless radial and axial coordinates, respectively
Re	Reynolds number
t	time
T	temperature
v	dimensional velocity
V	dimensionless velocity
α	thermal diffusivity
Γ	disk angular velocity ratio, ω_2/ω_1
δ	axial clearance between disk shrouds
θ	azimuthal coordinate
Θ	dimensionless temperature
v	kinematic viscosity
ρ	density
τ	dimensionless time
ψ	streamfunction
ω	angular velocity

Subscripts

1, 2	bottom and top disks, respectively
C, H	cold and hot, respectively
i, o	inner and outer, respectively
r	radial
θ	azimuthal
z	axial
T	temperature
RMS	root mean square

Superscripts

n	time discretization level

1. Introduction

Numerous engineering applications involve rotating disks, either singly or as facing disks or disk stacks. The applications include certain semiconductor manufacturing processes with rotating wafers, magnetic storage devices (disk drives), gas turbine engines, and other rotating machinery. Consequently, the fluid dynamics (and to a lesser extent the heat transfer) have been investigated for various geometries and ranges of conditions.

For the flow above a single spinning disk, von Karman (1921) recognized that a similarity solution of the Navier Stokes equations can be obtained provided that the disk is of infinite extent. Batchelor (1951) and Stewartson (1953) extended the similarity solutions to facing pairs of infinite ro-

* Corresponding author. E-mail: kball@burst.me.utexas.edu.

tating disks, but they differed on the predicted flow structure. Linear stability theory combined with the von Karman similarity transformation has been employed to assess instabilities and the presence of multiple solutions for both single and pairs of infinite disks (Holodniok et al., 1977; Holodniok et al., 1981; Anaturk and Szeri, 1992). Numerous single disk experiments have demonstrated the existence of three flow regimes near the disk surface: a laminar flow regime near the disk axis, a region of Ekman spirals at radial locations beyond a critical Re, and a turbulent flow region at radial locations beyond a higher critical Re (Chin and Litt, 1972; Wahal et al., 1993; Kobayashi, 1994). Szeri et al. (1983a, b) and Szeri and Adams (1978) assessed the effect of the infinite disk assumption and throughflow on finite open disk flow and stability characteristics, combining experiments with *B*-spline approximation Galerkin predictions. Several other works considering flow between rotating disks with or without throughflow have been reported (Lai et al., 1984; Elena and Schiestel, 1995; Nesreddine et al., 1995; Iacovides and Chew, 1993).

The flow between corotating disks has also been extensively studied. A summary of experimental and numerical observations available at the time is provided in Humphrey et al. (1991) and Abrahamson et al. (1991). Chang et al. (1989, 1990) reported two dimensional simulations of flow and heat transfer using a turbulence model, and obtained reasonable agreement with turbulent experimental data. Schuler et al. (1990), Humphrey et al. (1995), and Iglesias and Humphrey (1998) presented results of a combined experimental and numerical program to investigate the onset of instabilities and three dimensional laminar flow between corotating disks in a cylindrical enclosure. Their numerical results include both axisymmetric and three dimensional calculations, and provide insights to the three dimensional effects believed to be related to the appearance of foci of axial vorticity and the source of discrete frequencies found experimentally. However, they noted the disparity between experiment and simulation regarding the onset of instability and assume it to be due to the numerical diffusion in their control volume approach as well as the possibility of inadequate resolution in the three-dimensional model. Radel and Szeri (1997) used the geometry of Schuler et al. (1990) to perform three-dimensional steady state analyses using a *B*-spline numerical scheme and a very coarse grid resolution. They reported finding solutions that are axisymmetric but asymmetric about the axial midplane, in contradiction to the three-dimensional numerical results of Humphrey et al. (1995)

and Iglesias and Humphrey (1998) over the same range of conditions.

Fewer studies have focused on the flow between counter-rotating disks. Gan et al. (1994) and Kilic et al. (1994) considered the flow between counter-rotating disks in an annular enclosure, for several different values of the disk angular velocity ratio, Γ. They used a finite volume numerical approach combined with a turbulence model in an attempt to match their experimental data. The limiting case where one disk is held stationary, $\Gamma = 0$, was also studied by Randriamampianina et al. (1997), who used a two-dimensional spectral method at low Re (for flows believed to be laminar) and a finite-volume method employing a Reynolds stress transport model for the turbulent regime calculations at higher Re.

The numerical approach employed in the references above either used idealized geometric and/or similarity assumptions, low order spatial approximations, turbulence models, steady state assumptions, or combinations of these. Although at least two very recent studies using an axisymmetric application of spectral methods have considered transitional flow in a rotating disk system (Randriamampianina et al., 1997; Hill and Ball, 1997), it is believed that no previous three-dimensional studies have been undertaken to examine the flow and heat transfer (particularly the unsteady behavior and transition to chaos and turbulence) in a rotating disk geometry using a global spectral method approach. The work reported here was preceded by an axisymmetric study of the same counter-rotating disk problem (Hill and Ball, 1997). Additional details of the spectral simulations are also provided by Hill (1998).

2. Numerical approach

2.1. Model formulation

The coupled equations describing the time-dependent conservation of mass, momentum, and thermal energy for an incompressible fluid are solved subject to the imposed boundary conditions. The system of interest, shown in Fig. 1, is an annular region formed by two disks separated by a spacing of $2h$, with cylindrical shrouds attached to each disk at the inner and outer disk radii. (Since buoyancy forces are neglected, the orientation of the axis of rotation is arbitrary; for clarity in discussion disk (1) will be referred to as the bottom disk and disk (2) will be referred to as the top disk.) A small axial clearance, δ, separates the shrouds at the axial midplane
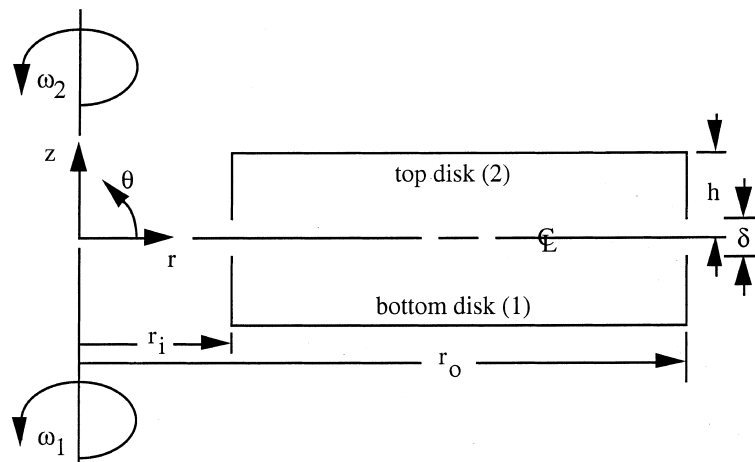

Fig. 1. Schematic of coordinate and physical system.

allowing each disk/shroud set to rotate freely from the other. The axial and radial velocities are assumed to be zero across the shroud clearance, thereby creating an enclosed system. This assumption is consistent with Kilic et al. (1994), who could control and thus eliminate net mass efflux through the axial clearance in their experimental apparatus. The azimuthal velocity is arbitrarily assumed to vary linearly between the shrouds; other profiles were used and the solutions were not found to be sensitive to the azimuthal velocity boundary condition across the relatively small shroud clearance. The bottom disk is held at the minimum system temperature and rotated at the maximum speed, and the top disk is held at the maximum system temperature and rotated in the direction opposite to that of the lower disk. For simplicity, the inner and outer shrouds and their separating clearance gaps are assumed to represent adiabatic boundaries. It is emphasized that the presence of the axial clearance between the shrouds and the boundary conditions imposed there are not necessitated by the numerical procedure employed in this study, but rather are included to match the geometry considered by Kilic et al. (1994).

The time-dependent three-dimensional momentum and thermal energy conservation equations are considered in a polar–cylindrical coordinate system assuming constant properties. The non-linear advective terms in the momentum equation are treated either in non-conservative form or in skew-symmetric form. Although for a collocation method the non-conservative form does not conserve kinetic energy and is therefore unstable over "long" time integrations, it requires the computation of fewer derivatives and thus less computer time than the skew-symmetric form. Since the two approaches provide equivalent statistical and average results (before the non-conservative computations become numerically unstable), the non-conservative form can be used for cases up to mildly chaotic flow. Above the mildly chaotic regime, the skew-symmetric form is used to ensure numerical stability over the time integration. The skew symmetric form is chosen over the more commonly used (and less computationally intensive) rotational form since the skew symmetric form has been found to converge faster to a grid independent solution (Zang, 1991). The form of the advective terms in the energy equation has been found to have no appreciable effect on the stability of the calculations and is thus left in the non-conservative form.

The following definitions are employed to simplify the non-dimensional form of the conservation equations.

$$C_1 = \left(\frac{r_o + r_i}{r_o - r_i} \right) \tag{1a}$$

$$C_2 = \left(\frac{r_i - r_o}{2} \right) \tag{1b}$$

$$C_3 = -C_2/h \tag{1c}$$

$$R = C_1 + \frac{r}{C_2} \tag{1d}$$

$$Z = -z/h \tag{1e}$$

$$\tau = \omega_1 t \tag{1f}$$

$$\nabla = \left(\frac{\partial}{\partial R} + \frac{1}{R - C_1} \right) \mathbf{e}_r + \left(C_3 \frac{\partial}{\partial Z} \right) \mathbf{e}_z + \left(\frac{1}{R - C_1} \frac{\partial}{\partial \theta} \right) \mathbf{e}_\theta \tag{1g}$$

$$\nabla^2 = \frac{\partial^2}{\partial R^2} + \frac{1}{R - C_1} \frac{\partial}{\partial R} + C_3^2 \frac{\partial^2}{\partial Z^2} + \frac{1}{(R - C_1)^2} \frac{\partial^2}{\partial \theta^2}. \tag{1h}$$

Using these definitions, the non-periodic coordinate directions, *r* and *z*, are mapped to the interval $[-1, 1]$ in *R* and *Z*, for convenience in applying the Chebyshev polynomial ex-

pansions to be discussed later. The dependent variables are non-dimensionalized by introducing length, time, and temperature scales based on the outer radius of the disks, the faster disk angular velocity, and the imposed temperature difference between the two disks. These scales are also used to define the remaining dimensionless parameters.

$$V_r = \frac{v_r}{\omega_1 C_2} \tag{2a}$$

$$V_\theta = \frac{v_\theta}{\omega_1 C_2} \tag{2b}$$

$$V_z = \frac{v_z}{\omega_1 C_2} \tag{2c}$$

$$\Theta = \frac{T - T_C}{T_H - T_C} \tag{2d}$$

$$P = \mathrm{Re} \left(\frac{C_2}{r_o} \right)^2 \frac{p}{\rho (\omega_1 C_2)^2} \tag{2e}$$

$$\mathrm{Re} = \frac{\omega_1 r_o^2}{\nu} \tag{2f}$$

$$\mathrm{Pr} = \frac{\upsilon}{\alpha} \tag{2g}$$

$$\mathrm{Pe} = \mathrm{Re}\,\mathrm{Pr}. \tag{2h}$$

The imposed temperature difference is assumed to be small enough so that corresponding changes in density are negligible, and buoyancy forces due to gravity or rotation are likewise negligible.

An Adams Bashforth/second order backward Euler (AB/2BE) time discretization is applied to the conservation equations, giving an implicit treatment of the diffusion terms and an explicit treatment of the advection terms that is second order accurate in time (Ehrenstein and Peyret, 1989). Upon performing the non-dimensionalization and the time discretization, the semi-discrete conservation equations (neglecting buoyancy) become:

Continuity:

$$\nabla \bullet \mathbf{V}^{n+1} = 0. \tag{3}$$

R-momentum:

$$\left[\nabla^2 - \frac{1}{(R - C_1)^2} - \mathrm{Re} \left(\frac{C_2}{r_o} \right)^2 \frac{3}{2\Delta\tau} \right] V_r^{n+1} - \frac{2}{(R - C_1)^2} \frac{\partial V_\theta^{n+1}}{\partial \theta}$$
$$= \frac{\partial P^{n+1}}{\partial R} + S_r^{n,n-1}. \tag{4}$$

θ-momentum:

$$\left[\nabla^2 - \frac{1}{(R - C_1)^2} - \mathrm{Re} \left(\frac{C_2}{r_o} \right)^2 \frac{3}{2\Delta\tau} \right] V_\theta^{n+1} + \frac{2}{(R - C_1)^2} \frac{\partial V_r}{\partial \theta}$$
$$= \frac{1}{(R - C_1)} \frac{\partial P^{n+1}}{\partial \theta} + S_\theta^{n,n-1}. \tag{5}$$

Z-momentum:

$$\left[\nabla^2 - \mathrm{Re} \left(\frac{C_2}{r_o} \right)^2 \frac{3}{2\Delta\tau} \right] V_z^{n+1} = C_3 \frac{\partial P^{n+1}}{\partial Z} + S_z^{n,n-1}. \tag{6}$$

Thermal energy:

$$\left[\nabla^2 - \mathrm{Pe} \left(\frac{C_2}{r_o} \right)^2 \frac{3}{2\Delta\tau} \right] \Theta^{n+1} = S_T^{n,n-1}. \tag{7}$$

The source terms, *S*, in Eqs. (4)–(7) include the explicit parts (the previous two time steps) of the non-linear advective

terms and the temporal terms (discretized in time) as follows (where x represents r, θ, and z for the radial, azimuthal, and axial directions, respectively).

$$S_x^{n,n-1} = \text{Re}\left(\frac{C_2}{r_o}\right)^2 \left[(\nabla \bullet \mathbf{VV} + \mathbf{V} \bullet \nabla\mathbf{V})_x^n - 0.5(\nabla \bullet \mathbf{VV}\right.$$

$$\left. + \mathbf{V} \bullet \nabla\mathbf{V})_x^{n-1}\right] - \text{Re}\left(\frac{C_2}{r_o}\right)^2 \left(\frac{4V_x^n - V_x^{n-1}}{2\Delta\tau}\right) \quad (8a)$$

$$S_T^{n,n-1} = \text{Pe}\left(\frac{C_2}{r_o}\right)^2 \left[2(\mathbf{V} \bullet \nabla\Theta)^n - (\mathbf{V} \bullet \nabla\Theta)^{n-1}\right]$$

$$- \text{Pe}\left(\frac{C_2}{r_o}\right)^2 \left(\frac{4\Theta^n - \Theta^{n-1}}{2\Delta\tau}\right). \quad (8b)$$

The pressure Poisson equation is generated by taking the divergence of the momentum equations, and since the divergence of the velocity is zero for incompressible flows, the following equation is obtained:

$$\nabla^2 P^{n+1} = -\nabla \bullet \mathbf{S}^{n,n-1}. \quad (9)$$

Eqs. (4) and (5) can not be directly solved for the V_r and V_θ velocity components since they appear implicitly in both equations. To decouple the equations, a transformation is introduced for the r and θ velocity components and directional unit vectors, following Patera and Orszag (1982). Further details can be found in Hill (1998).

The equations are solved subject to the boundary conditions that were discussed above for the system of interest (see Fig. 1). In dimensionless form, they are:

$Z = 1$:

$$V_r = V_z = \Theta = 0, \quad V_\theta = R - C_1. \quad (10a)$$

$Z = -1$:

$$V_r = V_z = 0, \quad \Theta = 1, \quad V_\theta = \Gamma(R - C_1). \quad (10b)$$

$R = 1$ and $Z > \delta/2h$:

$$V_r = V_z = \partial\Theta/\partial R = 0, \quad V_\theta = 1 - C_1. \quad (10c)$$

$R = 1$ and $Z < -\delta/2h$:

$$V_r = V_z = \partial\Theta/\partial R = 0, \quad V_\theta = \Gamma(1 - C_1). \quad (10d)$$

$R = -1$ and $Z > \delta/2h$:

$$V_r = V_z = \partial\Theta/\partial R = 0, \quad V_\theta = -(1 + C_1). \quad (10e)$$

$R = -1$ and $Z < -\delta/2h$:

$$V_r = V_z = \partial\Theta/\partial R = 0, \quad V_\theta = -\Gamma(1 + C_1). \quad (10f)$$

$R = 1, -1$ and $|Z| < \delta/2h$:

$$V_r = V_z = \partial\Theta/\partial R = 0, \quad V_\theta \text{ varies linearly.} \quad (10g)$$

No natural pressure boundary conditions exist to solve Eq. (9). Additionally, a method must be implemented to satisfy the incompressibility constraint of Eq. (3). Both problems are addressed using an influence matrix technique, which is described later. The influence matrix technique provides a direct non-iterative method to determine the pressure field that ensures that the incompressibility constraint is satisfied at every interior point and on the boundary.

To solve the conservation equations at each time step, a Fourier–Chebyshev collocation spectral method is used with no dealiasing (Canuto et al., 1988). Relative to a pseudospectral method, the collocation method provides a simpler approach to specifying the boundary conditions, a slight

improvement in convergence characteristics, and the elimination of the need to transfer back and forth between physical and wavenumber space for the non-periodic directions. The physical variables to be determined (velocities, pressure, and temperature) are represented by truncated series expansions of Chebyshev polynomials on a Gauss–Lobatto grid in both the radial and axial directions and by Fourier series on an evenly spaced grid in the periodic azimuthal direction. The form of the expansion for a generic variable, ϕ, is then:

$$\phi(R, Z, \theta, \tau) = \sum_{l=0}^{L-1} \sum_{m=0}^{M-1} \sum_{k_\theta=-K/2}^{K/2-1} \hat{\phi}_{lmk_\theta}(\tau) T_l(R) T_m(Z) \exp(ik_\theta\theta)$$

$$= \sum_{k_\theta=-K/2}^{K/2-1} \tilde{\phi}_{k_\theta}(R, Z, \tau) \exp(ik_\theta\theta) \quad (11)$$
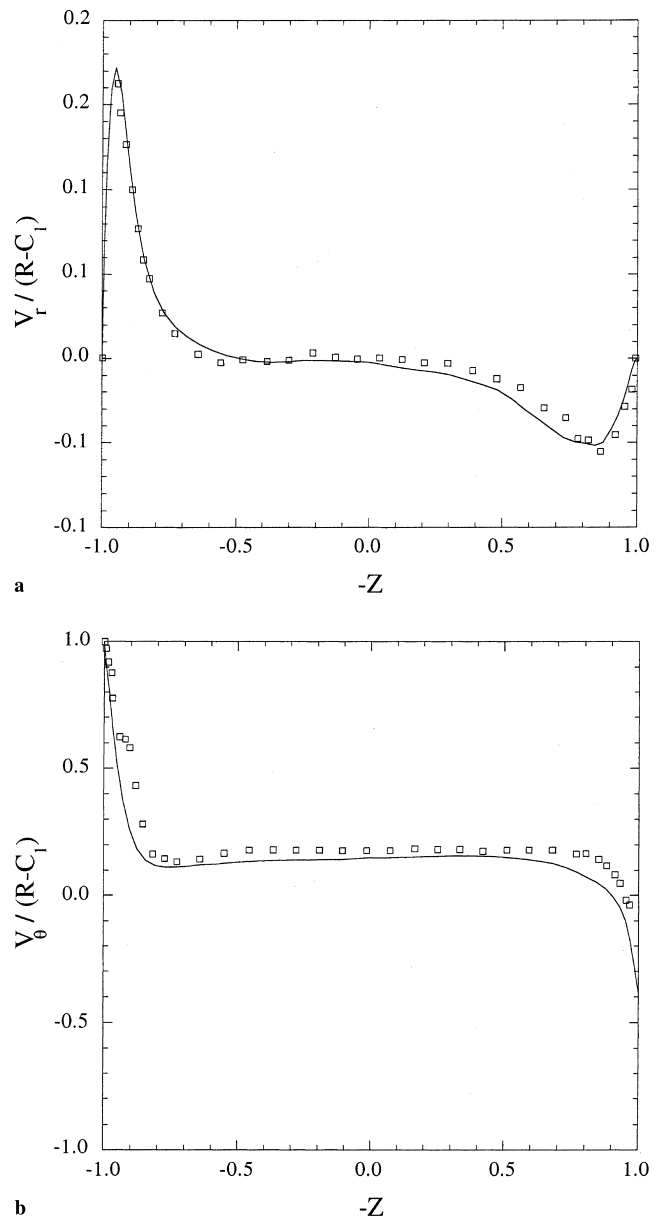

Fig. 2. Mean velocity profiles for $\text{Re} = 10^5$ and $\Gamma = -0.4$; symbols denote experimental data of Kilic et al. (1994); (a) V_r at $r/r_o = 0.85$, (b) V_θ at $r/r_o = 0.85$.

where i is the imaginary unit; L, M, and K are the number of grid points in the radial, axial, and azimuthal directions, respectively; $\hat{\phi}_{lmk_\theta}$ is the corresponding time-dependent Fourier–Chebyshev coefficient (to be determined); and T_l, T_m are the Chebyshev polynomials. This discretization approach enables one to generate first and second order spatial derivative operator matrices for the conservation equations in the r- and z-directions. Derivatives of the dependent variables in the non-periodic directions are thus evaluated by matrix products (Hill, 1998; Canuto et al., 1988; Ku et al., 1987).

Since the quantities of interest are expanded in Fourier series in the azimuthal direction, the simplest approach is to solve for the Fourier expansion coefficients. Upon performing the Fourier transform, the terms involving azimuthal derivatives can be represented by products of the Fourier coefficients and the corresponding Fourier wave numbers, which reduces the three-dimensional equations in physical space to a set of two-dimensional Helmholtz equations for each Fourier wave number.

The general form of the resulting set of discretized Helmholtz equations is as follows (where λ is zero for the pressure Poisson equation).

Table 1
Critical Re for onset of unsteady three-dimensional flow

Γ	Re_c
−1.0	1700
−0.4	4400
0.0	27 000

$$L_R\hat{\Phi} + \hat{\Phi}L_Z - \lambda\hat{\Phi} = \hat{S}^*, \tag{12}$$

where $\hat{S}^*$ is the original right-hand side source term modified to include the known quantities (boundary conditions) from the

Fig. 4. RMS velocity and temperature fluctuations in the r–z plane for $\Gamma = -1.0$ and Re = 1730, with maximum values given in parentheses; (a) $V_{\theta,\,RMS}(0.554)$, (b) $V_{r,\,RMS}(0.221)$, (c) $V_{z,\,RMS}(0.113)$, (d) $T_{RMS}(0.101)$.
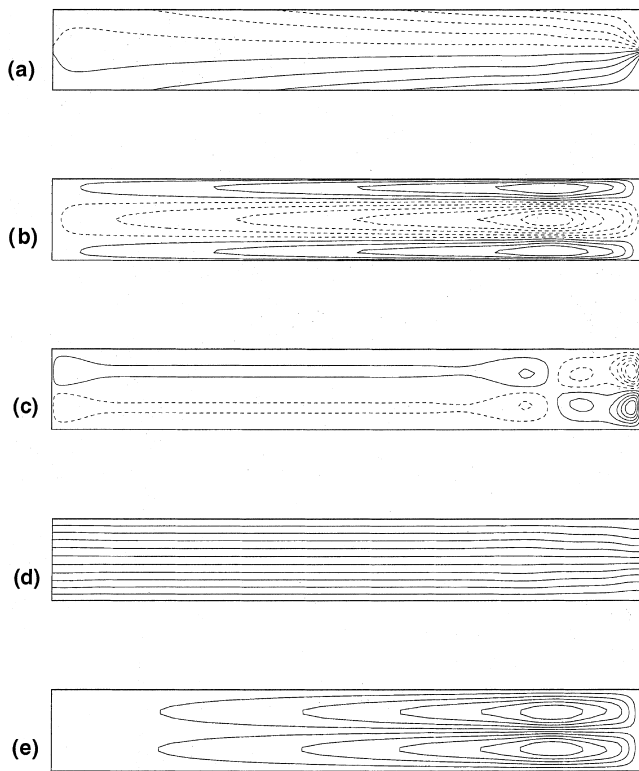

Fig. 3. Mean contours of flow variables in the r–z plane for $\Gamma = -1.0$ and Re = 1730, with maximum values given in parentheses; (a) $V_\theta(\pm 2.299)$, (b) $V_r(-0.231, 0.174)$, (c) $V_z(\pm 0.072)$, (d) T, (e) ψ.
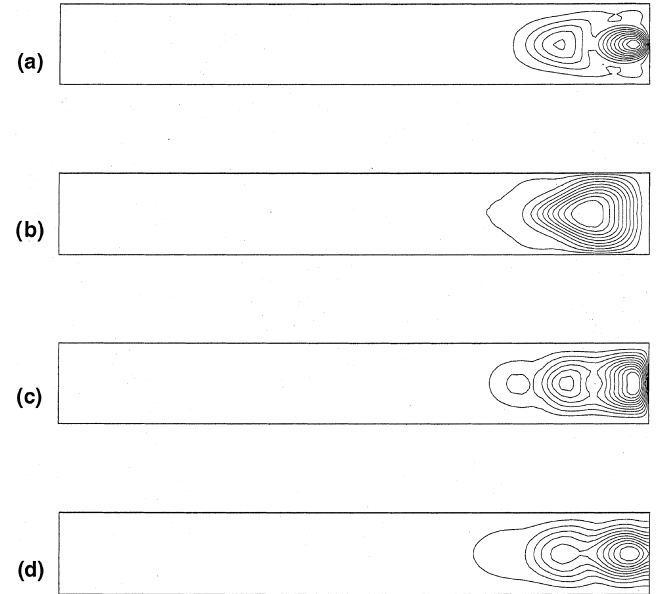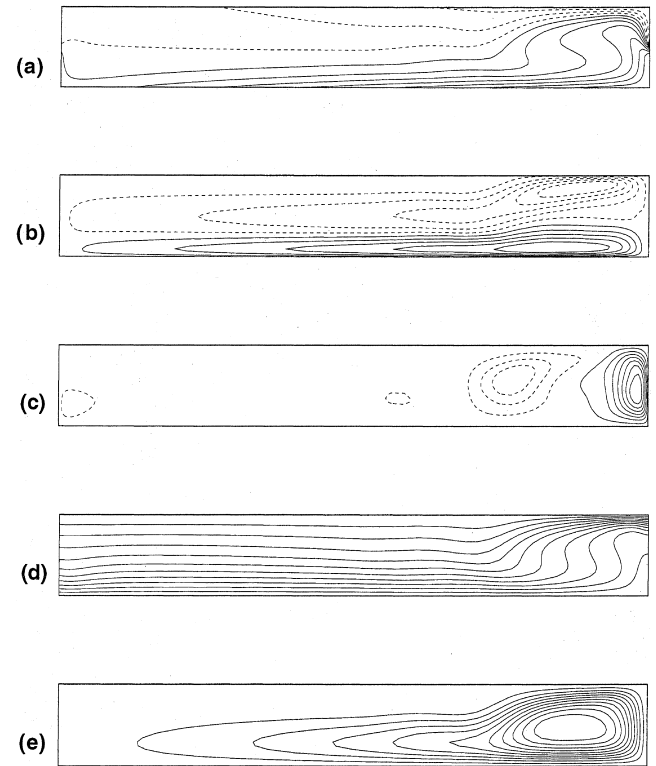

Fig. 5. Mean contours of flow variables in the r–z plane for $\Gamma = -0.4$ and Re = 4400, with maximum values given in parentheses; (a) $V_\theta(-0.920, 2.299)$, (b) $V_r(-0.278, 0.310)$, (c) $V_z(-0.099, 0.198)$, (d) T, (e) ψ.

left-hand side. Thus, a total of $5 \bullet K$ equations are generated (corresponding to the Fourier transforms of the three velocity components, pressure, and temperature for each of the K Fourier wavenumbers, k_θ). These equations are solved efficiently using matrix diagonalization techniques (Hill, 1998; Haidvogel and Zang, 1979; Yang and Shizgal, 1994).

To address the issue of the velocity–pressure coupling present in incompressible flows, an influence matrix technique is adopted. This approach is generally credited to Kleiser and Schumann (1980), who used it in a pseudospectral simulation of channel flow with one non-periodic direction. The method for one non-periodic direction is well summarized in Canuto et al. (1988). In a continuous representation of the Navier–Stokes equations, the influence matrix technique determines the pressures that ensure a divergence free condition throughout the solution domain by forcing the divergence of the velocity on the boundaries to be zero.

For the discretized problem, additional corrections throughout the domain are needed to force the divergence to machine precision zero due to the fact that the momentum equations are not satisfied on the boundary. The technique including the correction for the boundary momentum residuals for two non-periodic directions is described in detail by Tuckerman (1989) for Cartesian and cylindrical geometries using a pseudospectral method and by Madabhushi et al. (1993) for a Cartesian collocation implementation. Here and in Hill and Ball (1997) the correction is extended to a cylindrical collocation implementation.

The influence matrix technique without the boundary momentum correction has been used successfully by others (LeQuéré and Pécheux, 1989; Kuo and Ball, 1997; Ahmed and Ball, 1997); the motivation for not implementing the correction is primarily a factor of four savings in the memory required to store the influence matrix. However, early on in the study of flow in the counter-rotating disk system, it was determined that unbounded solutions became a severe problem under chaotic flow conditions unless the correction for the boundary momentum residuals was applied. A detailed summary of the influence matrix technique as used here in the study of transitional flows in cylindrical geometries is provided in Hill (1998).

2.2. Parallel implementation

Performing three-dimensional simulations of fluid flow and heat transfer requires considerable computer resources, both processing time and memory. The large memory requirement is a particular problem when using the influence matrix approach. To enable the numerical exploration of three-dimensional transitional flows, an efficient parallel implementation is desired to increase the wall clock time in which results can be obtained and discoveries made. The Fourier–Chebyshev spectral method described above has been parallelized for both shared memory and distributed memory platforms to perform the three-dimensional computations of transitional flow in cylindrical geometries. The approach to parallelizing the computations, as well as scaling and performance benchmarks, are described in detail in Hill (1998) and Hill and Ball (1999).

Briefly summarized, the approach to parallelizing the computations is based upon the factoring of the three-dimensional problem into a set of two-dimensional problems for each Fourier wavenumber, k_θ, described above. The resulting two-dimensional problems are then distributed among the available processing elements (PEs). The Cray proprietary SHMEM (logically shared memory) routines were used to perform the message passing required for the transient simulations. The results presented in this study were obtained using the Cray T3E-600 with 48 PEs at the University of Texas at Austin and the 512 PE Cray T3E at the Pittsburgh Supercomputing Center. Nearly linear scaling was achieved for computations using up to 128 PEs, with a small drop-off in performance beyond 128 PEs.
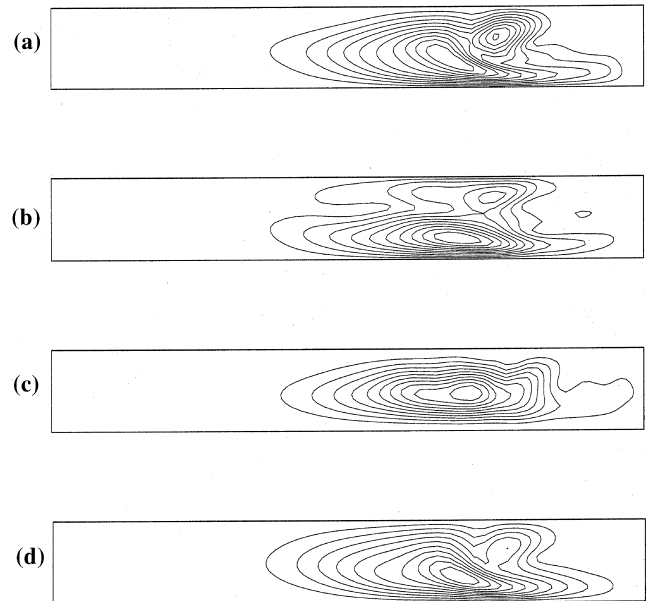

Fig. 6. RMS velocity and temperature fluctuations in the r–z plane for $\Gamma = -0.4$ and Re = 4400, with maximum values given in parentheses; (a) $V_{\theta,\,\text{RMS}}(0.090)$, (b) $V_{r,\,\text{RMS}}(0.054)$, (c) $V_{z,\,\text{RMS}}(0.028)$, (d) $T_{\text{RMS}}(0.055)$.
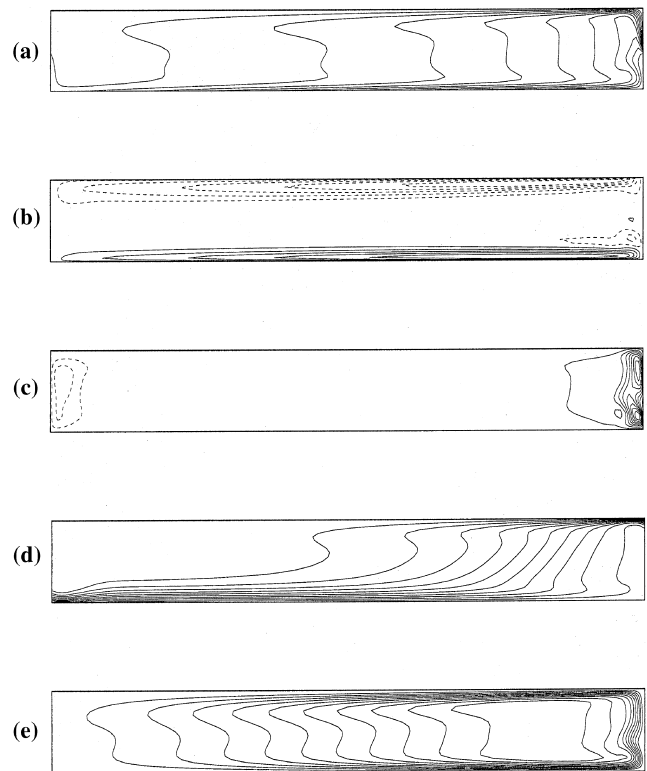

Fig. 7. Mean contours of flow variables in the r–z plane for $\Gamma = 0$ and Re = 27000, with maximum values given in parentheses; (a) $V_\theta(2.299)$, (b) $V_r(-0.246, 0.269)$, (c) $V_z(-0.049, 0.143)$, (d) T, (e) ψ.
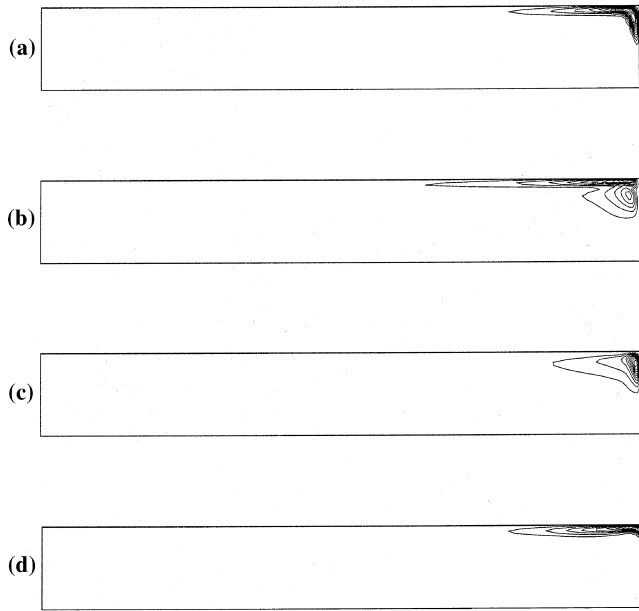
Fig. 8. Rms velocity and temperature fluctuations in the r–z plane for $\Gamma = 0$ and Re = 27000, with maximum values given in parentheses; (a) $V_{\theta, \text{RMS}}(0.121)$, (b) $V_{r, \text{RMS}}(0.030)$, (c) $V_{z, \text{RMS}}(0.035)$, (d) $T_{\text{RMS}}(0.066)$.

2.3. Solution procedure

At each time step, the solution proceeds by first solving for the temperature field. Assuming boundary pressures of zero, a pressure field and accompanying V_r and V_z are calculated. Then employing the pre-determined influence matrix, the corrections to the boundary pressures are determined that will ensure a divergence-free velocity field. Using these boundary pressures, an implicitly determined pressure field, and finally the new V_r, V_z, and V_θ values, are calculated at the new time step.

A typical approach to generating three-dimensional results is first to perform a two-dimensional simulation, assuming the flow and temperature field to be axisymmetric. Then this solution is wrapped around to each azimuthal plane as a starting condition for the three-dimensional computations. This solution is then randomly perturbed in the first time step to induce a small three-dimensional disturbance on top of the base flow. The perturbation is typically in the form of a ±0.1–1.0% disturbance applied to the velocity component source terms. Without this disturbance, the solution would remain axisymmetric due to the perfect separation of the Fourier modes.

It should be noted that the Re used to obtain the two-dimensional initial condition may or may not correspond to the Re for the three-dimensional simulation. If at the Re of interest the flow is actually axisymmetric, the disturbance will die out and azimuthal derivatives will tend to zero. However, if the flow is three-dimensional, the flow will evolve from the slightly disturbed axisymmetric state to the preferred three-dimensional state corresponding to that Re. Once a solution is available in which three-dimensional characteristics are pres-
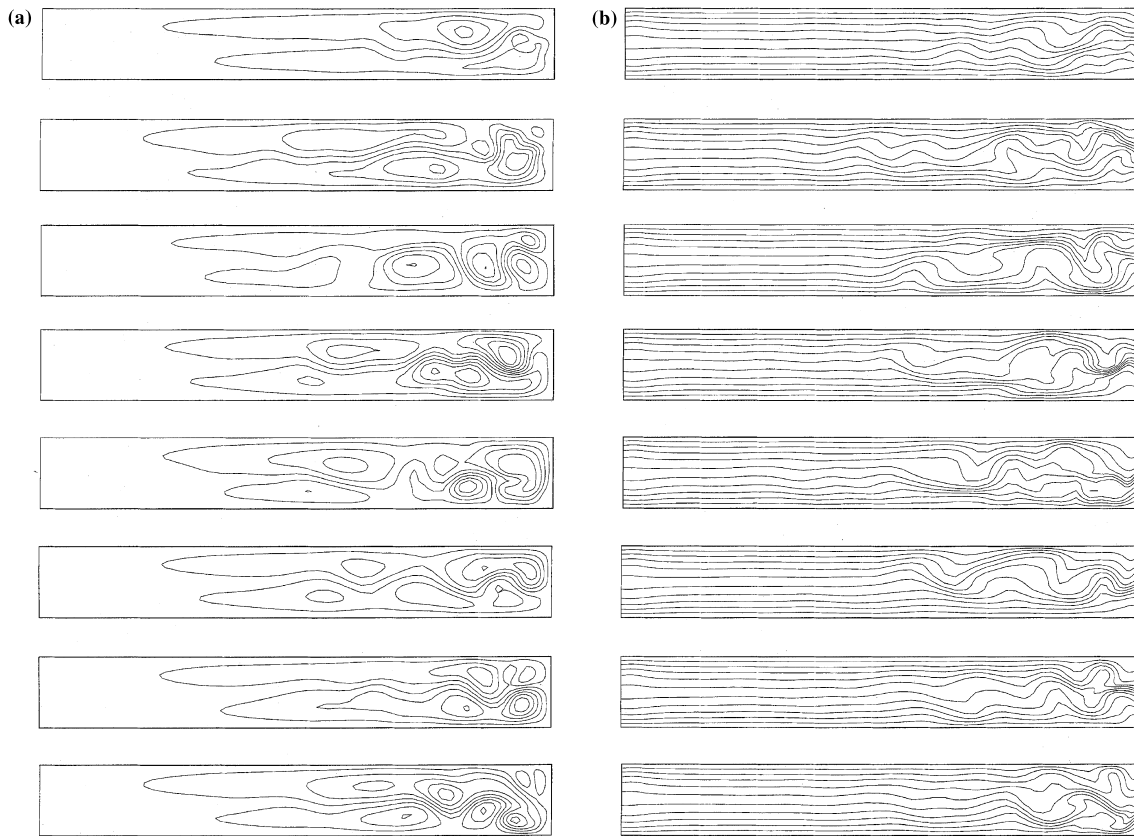

Fig. 9. (a) Instantaneous secondary flow streamlines in the r–z plane for $\Gamma = -1.0$ and Re = 4500, at eight equally spaced azimuthal locations ($\Delta\theta = \pi/4$). (b) Instantaneous temperature contours in the r–z plane for $\Gamma = -1.0$ and Re = 4500, at eight equally spaced azimuthal locations ($\Delta\theta = \pi/4$).

ent, that solution may be used as initial conditions for solutions at other Re and/or other grid resolutions (following proper interpolation of the Fourier and Chebyshev expansion coefficients onto the new grid).

To generate the results reported here, different grid resolutions were employed depending upon the specific case. For $\Gamma = -1.0$, the grid resolutions (r, z, θ) were $73 \times 31 \times 128$ for $\text{Re} = 1730$ and $73 \times 31 \times 512$ for $\text{Re} = 4500$. For $\Gamma = -0.4$, the grid resolutions were $73 \times 31 \times 64$ for $\text{Re} = 4400$ and $73 \times 31 \times 384$ for $\text{Re} = 12000$. For $\Gamma = 0.0$, the grid resolutions were $73 \times 31 \times 128$ for $\text{Re} = 27000$ and $97 \times 41 \times 256$ for $\text{Re} = 70000$. For the lower Re cases considered, the grid resolutions were deemed to be adequate when the numerically determined critical values of Re became insensitive to further increases in grid resolution, allowing Re_c to be determined to within 3–5% as discussed later. For the higher Re cases considered, the grid resolutions were deemed to be adequate when no qualitative changes in the flow behavior were observed, and quantitative changes (in the mean statistics) were small. It is noted that when smaller grids were employed, problems were encountered in solving the energy equation; namely, local temperature values within the computational domain that exceeded the range of the boundary conditions were encountered due to insufficient resolution.

3. Results

3.1. Isothermal flow for $\Gamma = -0.4$, $Re = 10^5$

To provide a benchmark for the numerical approach used in this study, results are presented for the isothermal flow for $\Gamma = -0.4$ and $\text{Re} = 10^5$ and are compared with experimental

data taken from the literature (Kilic et al., 1994). In Fig. 2, the time and azimuthally averaged axial variation of V_r and V_θ are shown at $r/r_o = 0.85$. Each profile is normalized by $(R - C_1)$, which is the local V_θ for disk (1), and the faster bottom disk is on the left. As noted by Hill and Ball (1997), the mean velocity profiles between the two disks using two-dimensional (axisymmetric) simulations do not agree well with the experimental data from Kilic et al. (1994) for this case; thus, it is deemed to be an important benchmark for the three-dimensional simulation.

An important feature of this flow is the presence of a stagnation point along the upper disk, where the centrifugally driven (radially outward) flow along the bottom disk turns upward at the sidewall, then flows radially inward along the upper disk, and meets the centrifugally driven (radially outward) flow along the more slowly rotating upper disk. The mean location of the stagnation point can be detected by a change in sign in the mean radial velocity component near the upper disk.

In Fig. 2(a), the mean V_r is negative near the upper disk, indicating that the flow there is radially inward. The mean radial velocity profile at $r/r_o = 0.8$ (not shown) is positive near the upper disk, indicating that the flow is radially outward at that location. Thus, the stagnation point occurs (in the mean) between $0.8 < r/r_o < 0.85$, which is consistent with the experimental results of Kilic et al. (1994). In addition to properly bracketing the location of the mean stagnation point, the magnitude of V_r in the Ekman layers on each disk is shown to be very well predicted.

Fig. 2(b) shows axial profiles of the mean V_θ at $r/r_o = 0.85$, accompanied by the experimental data from Kilic et al. (1994). The numerical results match the experimental data much better than in the case of the two-dimensional simulations (Hill and Ball, 1997). The rotation of the core region is well represented, both in magnitude and trend. In assessing the agreement with the experimental data, it is noted that while Kilic et al. (1994) provide some indication of the uncertainties for various system inputs to their experiments (such as probe point
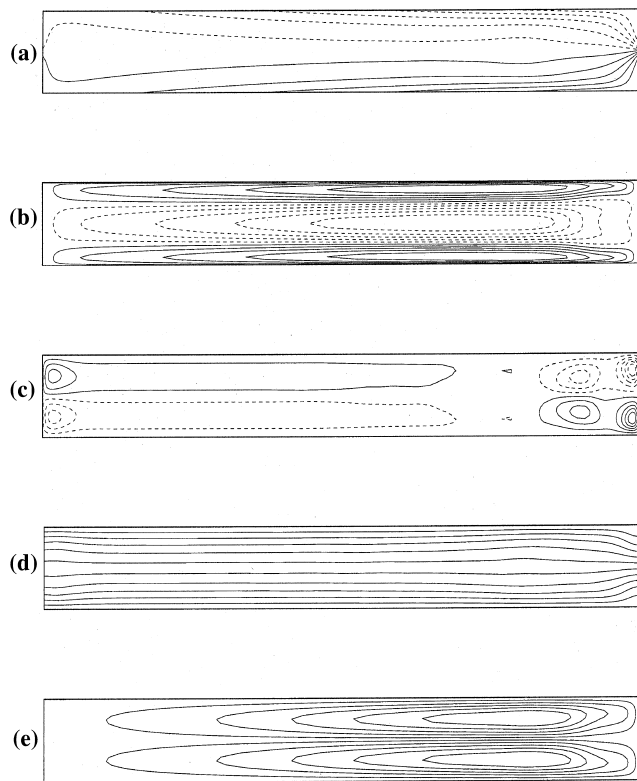

Fig. 10. Mean contours of flow variables in the r–z plane for $\Gamma = -1.0$ and $\text{Re} = 4500$, with maximum values given in parentheses; (a) $V_\theta (\pm 2.299)$, (b) $V_r (\pm 0.221)$, (c) $V_z (\pm 0.065)$, (d) T, (e) ψ.
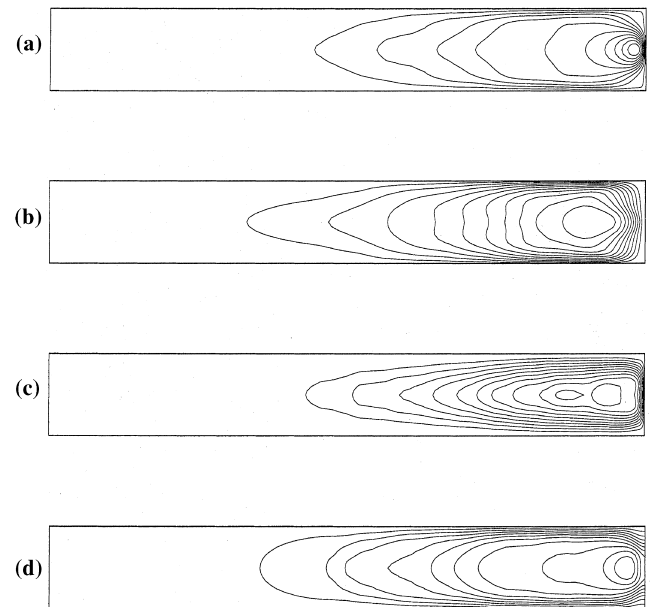

Fig. 11. RMS velocity and temperature fluctuations in the r–z plane for $\Gamma = -1.0$ and $\text{Re} = 4500$, with maximum values given in parentheses; (a) $V_{\theta, \text{RMS}}(0.695)$, (b) $V_{r, \text{RMS}}(0.316)$, (c) $V_{z, \text{RMS}}(0.217)$, (d) $T_{\text{RMS}}(0.142)$.

positioning), they have not quantified the experimental uncertainties of the flow velocity measurements. The high level of agreement with the experimental data also provides an indication that the numerical treatment of the shroud clearance boundary conditions is consistent with the experimentally realized clearance boundary conditions.

Neither the steady two-dimensional finite difference numerical simulations of Kilic et al. (1994) using a turbulence model nor the unsteady two-dimensional spectral simulations of Hill and Ball (1997) could match the experimental data for $\Gamma = -0.4$ and $Re = 10^5$. Thus, it is strongly concluded that the problems associated with matching the experimental data when performing an axisymmetric simulation for this counter rotating disk geometry are due to the axisymmetry assumption itself. Although, on average, the azimuthal derivatives are zero, excluding them from the numerical model removes an important player from the physical problem leading to erroneous results.

3.2. Transition to unsteady three-dimensional flow

For all of the cases considered in this study, the initial transition in the flow from the steady axisymmetric state with increasing Re is to an unsteady three-dimensional flow. Critical values of Re were determined by increasing Re in small increments following the procedure described previously. The Re_c so determined are considered to be accurate to within 3–5%, and are given in Table 1.

$\Gamma = -1.0$: Fig. 3 shows mean contours (dashed lines indicate negative contour levels) of the three velocity components, temperature, and secondary flow streamfunction in the r–z

plane for $Re = 1730$. At this Re, the flow has just undergone a transition to unsteady three-dimensional flow from a steady two-dimensional flow at just below $Re_c = 1700$. The mean flow is characterized by radial outflow on both disks that meets to form an inflowing free shear layer in the midplane, with rotating fluid on either side (Fig. 3(a),(b) and (c)). The mean secondary flow (in the r–z plane) thus consists of two large counter-rotating circulations, with the centers of rotation occurring near the outer sidewalls (Fig. 3(e)). At this relatively low Re, the flow is primarily parallel to the disks (except where it turns at the sidewalls) and the temperature distribution is characteristic of diffusion in the axial direction (Fig. 3(d)).

Contours of the RMS velocity and temperature fluctuations in the r–z plane for $Re = 1730$ are shown in Fig. 4. It is apparent that the unsteadiness originates at the outer sidewalls where the two radially outward boundary layers meet and form the free shear layer noted above. The extent of the fluctuations is limited to a small region near the outer sidewalls, beyond approximately $r/r_o = 0.80$. Qualitatively, the distribution of $V_{\theta, RMS}$, $V_{z, RMS}$, and T_{RMS} are similar, with two peaks occurring along the midplane; a strong peak very near the outer sidewalls ($r/r_o \approx 0.97$) and a second peak near the centers of circulation ($r/r_o \approx 0.88$). The distribution of $V_{r, RMS}$ has only one peak, occurring just outward of the centers of circulation ($r/r_o \approx 0.92$).

$\Gamma = -0.4$: Fig. 5 shows mean contours of the flow variables in the r–z plane for $Re = 4400$. At this Re, transition to unsteady three-dimensional flow from a steady two-dimensional flow at $Re = 4300$ has just occurred. The stronger counter-clockwise secondary circulation induced by the rotation of the bottom disk is evident in Fig. 5(e), resulting in the relatively
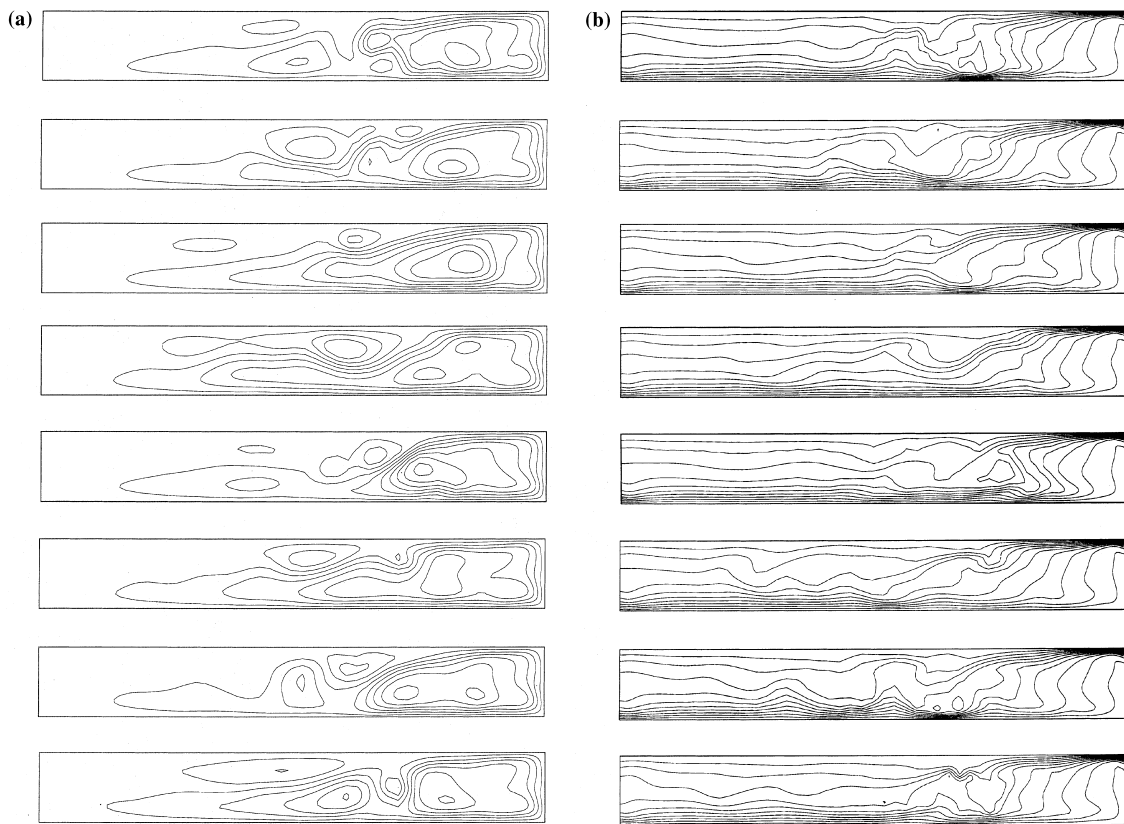

Fig. 12. (a) Instantaneous secondary flow streamlines in the r–z plane for $\Gamma = -0.4$ and $Re = 12000$, at eight equally spaced azimuthal locations ($\Delta\theta = \pi/4$). (b) Instantaneous temperature contours in the r–z plane for $\Gamma = -0.4$ and $Re = 12000$, at eight equally spaced azimuthal locations ($\Delta\theta = \pi/4$).

small temperature gradients near the outer portion of the lower disk and the large temperature gradients near the outer portion of the slower rotating top disk. Where the counterclockwise circulation and the weaker clockwise circulation meet near the top disk, fluid is forced downward into the core region between the two disks. The center of the counterclockwise circulation occurs at approximately $r/r_o = 0.90$. The resulting free shear layer is inclined at an angle of approximately $40°$ to the horizontal midplane.

Contours of the RMS velocity and temperature fluctuations in the r–z plane for Re = 4400 are shown in Fig. 6. The peak RMS levels occur for each variable along the path of the free shear layer, which separates from the upper disk near $r/r_o = 0.80$ and flows downward along an inclined path as described above. The contours for $V_{\theta,\text{RMS}}$, $V_{r,\text{RMS}}$, and T_{RMS} all exhibit a two-lobed structure, with the larger peak occurring downstream of the first peak in the direction of the free shear layer. The distribution of $V_{z,\text{RMS}}$ has only one peak, near $r/r_o = 0.75$ at the midplane, where the free shear layer has its maximum curvature as it straightens out to flow radially inward along a nearly horizontal path. The spatial extent of the RMS fluctuations is considerably larger than the $\Gamma = -1.0$ case, occupying approximately half of the annular volume.

$\Gamma = 0.0$: Fig. 7 shows mean contours of the flow variables in the r–z plane at eight equally spaced azimuthal locations for Re = 27000. As above, the flow has just experienced a transition to unsteady three-dimensional flow from a steady two-dimensional flow at lower Re. In this case, a single counter-rotating circulation results from the rotation of the bottom disk, and is largely confined to the two boundary layers along each disk (Fig. 7(e)). The radial component of velocity in the core region is negligible (Fig. 7(b)), and the

angular momentum in the core region is horizontally stratified (Fig. 7(a)). Sharp gradients in the temperature field develop along the upper disk near the outer sidewall where the relatively cold fluid originating from the bottom impinges on the hot upper disk. In similar fashion, sharp temperature gradients also develop along the bottom disk near the inner sidewall where the relatively hot fluid originating from the top impinges on the cold bottom disk (Fig. 7(d)).

Contours of the RMS velocity and temperature fluctuations in the r–z plane for Re = 27000 are shown in Fig. 8. The only significant RMS fluctuation levels occur in a small region along the upper disk adjacent to the outer sidewall, extending radially inward to about $r/r_o = 0.8$.

3.3. Turbulent flow at 3 Re_c

To study the development of turbulence in the counter-rotating disk system, the flow at values of Re that are approximately three times the respective critical values are considered for each Γ. In all three cases, the flow is chaotic (as evidenced by broadband power spectra) and may be considered to be weakly turbulent; the flow appears to become increasingly disordered as Γ increases in magnitude at fixed Re.

$\Gamma = -1.0$: In Fig. 9(a) and (b), the secondary flow streamlines and temperature contours in the r–z plane are presented for Re = 4500, at eight equally spaced azimuthal locations at a fixed instant in time. This is equivalent to viewing a sequence of instantaneous snapshots separated by small fixed increments in time. The chaotic nature of the flow is evident. The flow is characterized by a large number of pockets of fluid circulation, resulting in significant oscillations in the flow and temperature fields in both space and time. The flow is most chaotic in the region nearest to the outer sidewalls, where the angular velocity of the disks is largest.

Fig. 10 shows mean contours of the flow variables in the r–z plane. When averaged over long enough periods of time or large enough ensembles, the flow with $\Gamma = -1.0$ exhibits midplane symmetry. The mean flow field is qualitatively very
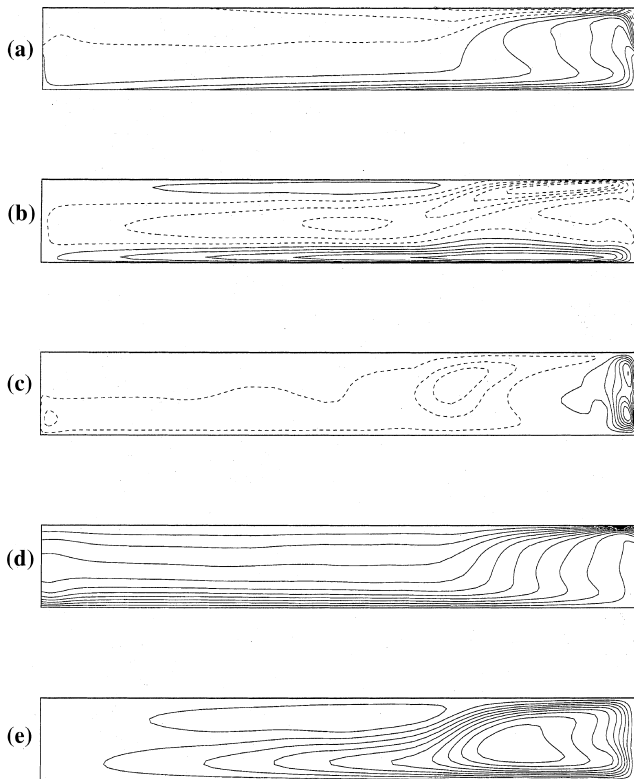

Fig. 13. Mean contours of flow variables in the r–z plane for $\Gamma = -0.4$ and Re = 12000, with maximum values given in parentheses; (a) $V_\theta(-0.920, 2.299)$, (b) $V_r(-0.260, 0.298)$, (c) $V_z(-0.069, 0.170)$, (d) T, (e) ψ.
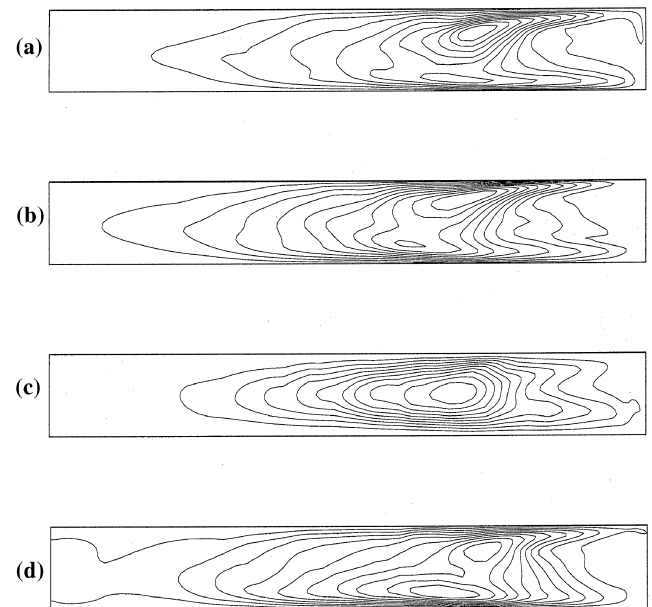
Fig. 14. RMS velocity and temperature fluctuations in the r–z plane for $\Gamma = -0.4$ and Re = 12000, with maximum values given in parentheses; (a) $V_{\theta,\text{RMS}}(0.210)$, (b) $V_{r,\text{RMS}}(0.129)$, (c) $V_{z,\text{RMS}}(0.074)$, (d) $T_{\text{RMS}}(0.103)$.
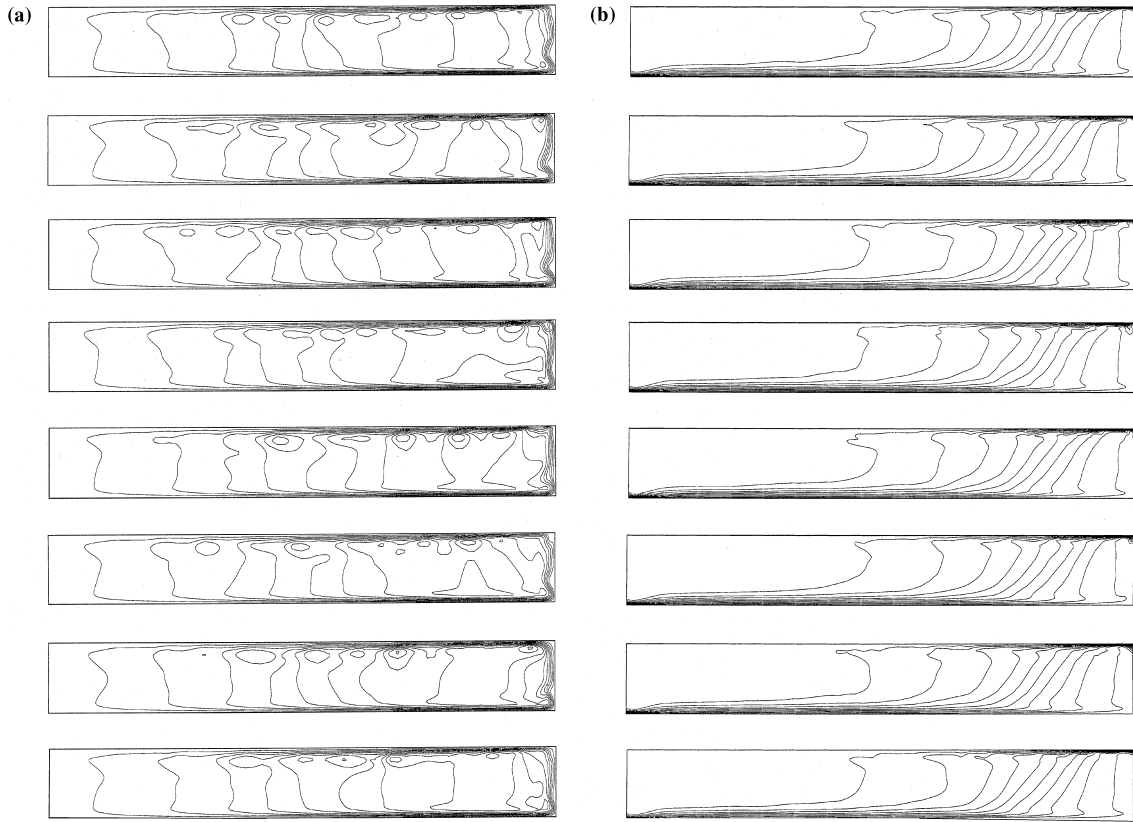
(a)

(b)

Fig. 15. (a) Instantaneous secondary flow streamlines in the r–z plane for $\Gamma = 0$ and Re = 70000, at eight equally spaced azimuthal locations ($\Delta\theta = \pi/4$). (b) Instantaneous temperature contours in the r–z plane for $\Gamma = 0$ and Re = 70000, at eight equally spaced azimuthal locations ($\Delta\theta = \pi/4$).

similar to the lower Re flow presented in Fig. 3, only more vigorous. Also, the centers of the two counter-rotating circulations have moved radially inward slightly, to about $r/r_{\mathrm{o}} = 0.82$.

Contours of the RMS velocity and temperature fluctuations in the r–z plane for Re = 4500 are shown in Fig. 11. As with the lower Re case shown in Fig. 4, the unsteadiness originates at the outer sidewalls where the free shear layer develops. However, in contrast to that case, the spatial extent of the fluctuations is considerably larger, occupying more than half of the annular volume. Remnants of the two-lobed structure in $V_{z,\mathrm{RMS}}$, and T_{RMS} remain, though this is no longer a dominant feature.

$\Gamma = -0.4$: In Fig. 12(a) and (b), the secondary flow streamfunction and temperature contours in the r–z plane are presented for Re = 12000, at eight equally spaced azimuthal locations at a fixed instant in time. Again, the chaotic nature of the flow is evident, and is characterized by numerous pockets of fluid advecting with the flow (Fig. 12(a)). These pockets of fluid result in considerable distortion of the temperature field (Fig. 12(b)). It is also evident upon inspection of Fig. 12(a) that the location of the stagnation point on the upper disk, where the radially opposing boundary layer flows meet to form the downward inclined shear layer, fluctuates wildly. The penetration depth of the shear layer (before it straightens out to flow radially inward along a horizontal path) also varies considerably, resulting in fluctuations in the temperature gradients along the bottom disk in the region below the free shear layer ($r/r_{\mathrm{o}} \approx 0.65$ to $r/r_{\mathrm{o}} \approx 0.75$; Fig. 12(b)).

Fig. 13 shows mean contours of the flow variables in the r–z plane. As with the $\Gamma = -1.0$ case, the mean flow at 3 • Re$_{\mathrm{c}}$ is qualitatively similar to that near Re$_{\mathrm{c}}$, only more vigorous. In Fig. 13, the clockwise circulation along the upper disk at
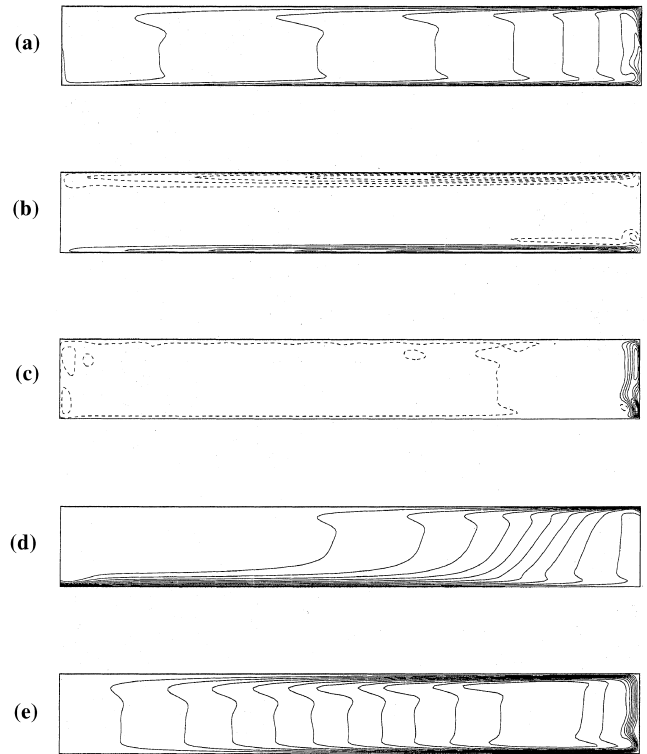
(a)

(b)

(c)

(d)

(e)

Fig. 16. Mean contours of flow variables in the r–z plane for $\Gamma = 0$ and Re = 70000, with maximum values given in parentheses; (a) $V_{\theta}(2.299)$, (b) $V_r(-0.238, 0.272)$, (c) $V_z(-0.039, 0.160)$, (d) T, (e) ψ.
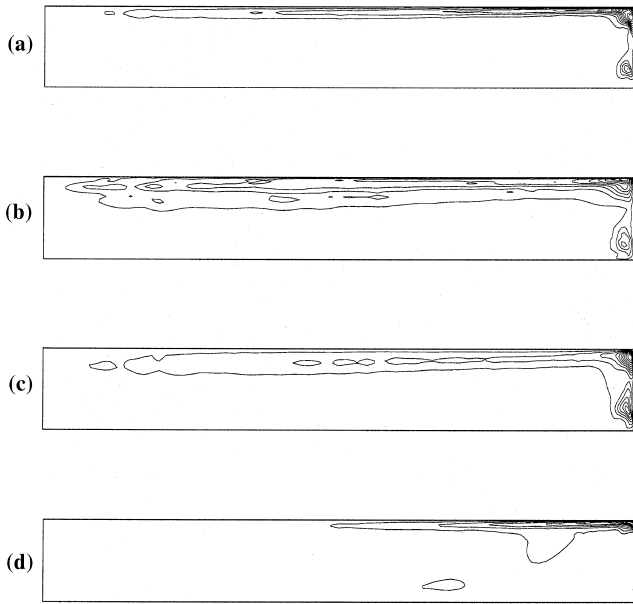
Fig. 17. RMS velocity and temperature fluctuations in the r–z plane for $\Gamma = 0$ and Re = 70000, with maximum values given in parentheses; (a) $V_{\theta,\,RMS}(0.269)$, (b) $V_{r,\,RMS}(0.066)$, (c) $V_{z,\,RMS}(0.077)$, (d) $T_{RMS}(0.136)$.

Fig. 18. Radial variation of mean Nu for $\Gamma = -1.0$.

$r/r_o < 0.8$ is now well defined, and the center of the counter-clockwise circulation has shifted inward slightly. The temperature gradients on the upper disk near the outer sidewall are also significantly higher (Fig. 13(d)).

In Fig. 14, the RMS velocity and temperature fluctuations for Re = 12000 are presented. Significant fluctuation levels occur throughout the entire annular volume, with peaks occurring along the mean path of the free shear layer, penetrating all the way down to the bottom disk.

$\Gamma = 0.0$: In Fig. 15(a) and (b), the secondary flow stream-function and temperature contours in the r–z plane are presented for Re = 70000 at eight equally spaced azimuthal locations at a fixed instant in time. The flow is observed to be chaotic, with numerous smaller pockets (relative to the previous two cases) of circulating fluid moving radially inward along the upper disk. The corresponding mean flow field is shown in Fig. 16. Once again, it is qualitatively similar to the flow shown in Fig. 7 and discussed earlier. However, the RMS velocity and temperature fluctuations, shown in Fig. 17, are now at significant levels over the entire region along the upper disk. The boundary layer along the bottom disk is still fairly steady at this Re.

3.4. Heat transfer results

The local values of Nu (based on the disk spacing, $2h$) are obtained by averaging the profiles over all azimuthal planes at a given radius for several snapshots and then averaging over the snapshots to obtain a single curve for each Re and each disk. For $\Gamma = -1.0$, the profiles on each disk may also be combined to generate a single curve corresponding to both disks due to the midplane symmetry.

Fig. 18 provides a plot of the radial variation of the average heat transfer rate for Re = 1730 and 4500 and for $\Gamma = -1.0$. Near the outer radius, the heat transfer rate is very small due to the turning of the flow and the resultant decrease in temperature gradients as shown in Fig. 3 and Fig. 10. Moving radially inward on each disk, the heat transfer rate increases rapidly to a peak around $r/r_o = 0.85$. It then drops to a relatively constant rate that is dependent on Re, followed by an-
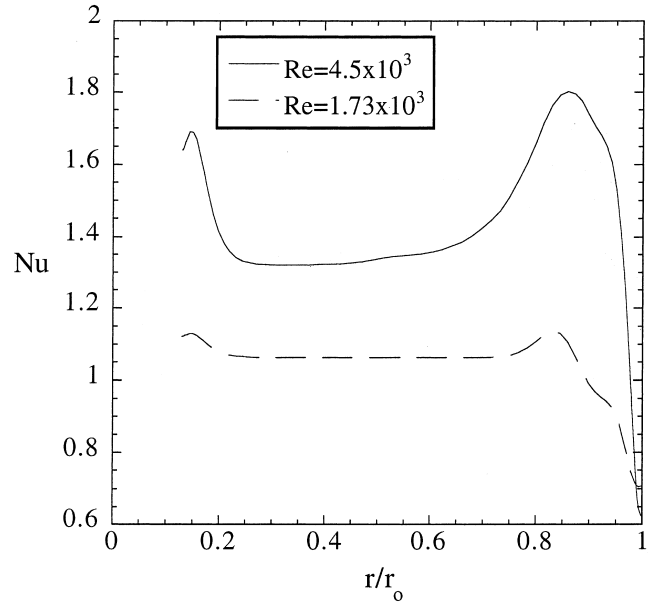
other rise near the inner radius caused here by the turning flow. The peak in the heat transfer near $r/r_o = 0.85$ is attributed to the unsteadiness and mixing in the flow at that location, as seen in the RMS profiles of Fig. 4 and Fig. 11. Similarly, the relatively constant heat transfer rate midway between the inner and outer radius is attributed to the flow being much less unsteady there. The increase in magnitude and broadening of the peak near $r/r_o = 0.85$ for Re = 4500 is due to the more chaotic flow (Fig. 11) and resulting increase in mixing for higher Re.

The heat transfer rates for $\Gamma = -0.4$ and 0.0 are provided in Figs. 19 and 20. For these cases the radial profiles of Nu reflect
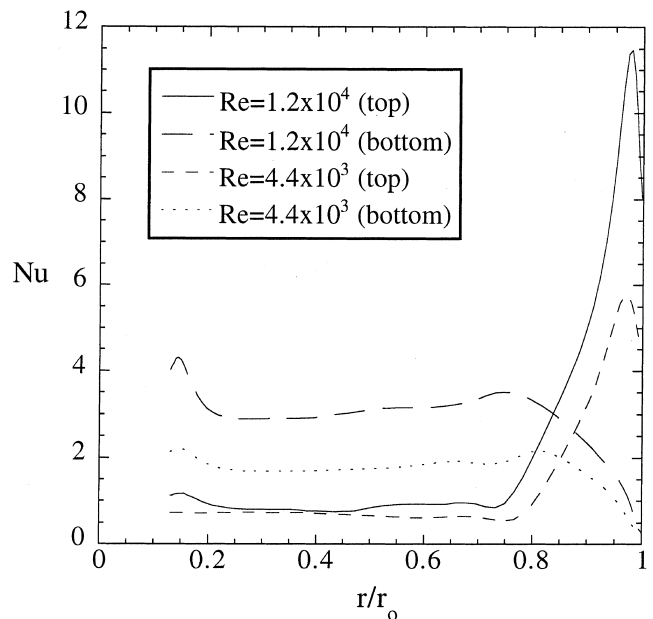

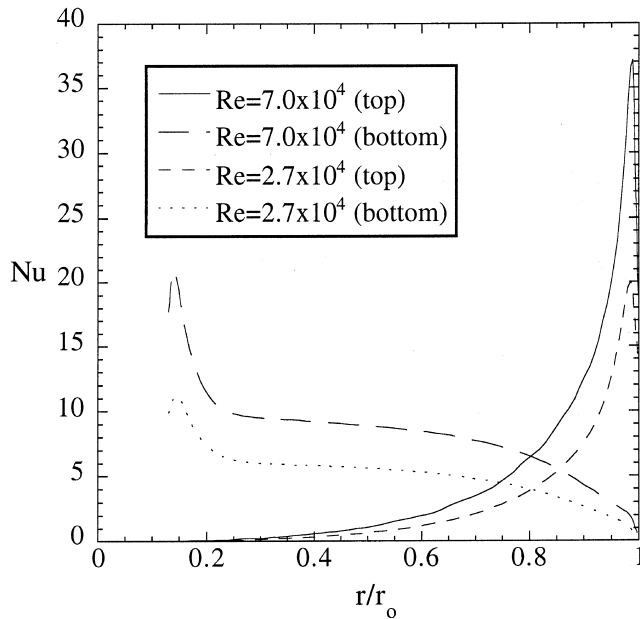Fig. 19. Radial variation of mean Nu for $\Gamma = -0.4$.

Fig. 20. Radial variation of mean Nu for $\Gamma = 0$.

the behavior of the mean flow and are not dominated by turbulent mixing. In both cases a very strong counter-clockwise rotating secondary flow directly strikes the top disk near the outer radius resulting in the highest heat transfer rates along the top disk. This flow structure similarly results in a very low heat transfer near the outer radius of the bottom disk. At smaller radial locations the heat transfer rate is relatively constant with radial position for $\Gamma = -0.4$, whereas it exhibits an asymptotic decrease(increase) for the top(bottom) disk in the case of $\Gamma = 0.0$.

4. Conclusion

A Fourier–Chebyshev collocation spectral method is used to simulate the three-dimensional unsteady flow and heat transfer inside a cylindrical annular enclosure. Turbulent flows with Reynolds numbers up to $3 \bullet Re_c$ are simulated, for cases with both disks rotating at the same speed, $\Gamma = -1.0$, with one disk rotating slower than the other, $\Gamma = -0.4$, and with one stationary disk, $\Gamma = 0$. Solutions are obtained over a wide range of Re including the transition from laminar flow, and the benchmark isothermal results agree well with published experimental data. Differences with previously reported numerical results assuming axisymmetry or using turbulence models are also discussed. The heat transfer rates between the disks are also obtained, showing the effects of transition to turbulence. As the rotational speed of both disks is increased proportionally (thereby maintaining the same speed ratio but increasing the system Re), the flow undergoes a transition from steady to unsteady and chaotic conditions, and the three-dimensional nature of the flow is clearly observable. The fluctuations throughout the flow are associated with a free shear layer that arises from the boundary layers over each disk for the cases $\Gamma = -1.0$ and $\Gamma = -0.4$. For $\Gamma = 0.0$, the fluctuations are limited in extent to the boundary layer over the upper disk. Finally, the flow is noticeably more chaotic at the same Re as the magnitude of Γ increases.

References

Abrahamson, S.D., Chiang, C., Eaton, J.K., 1991. Flow structure in head-disk assemblies and implications for design. Advances Information Storage Systems 1, 111–132.

Ahmed, I., Ball, K.S., 1997. Spectral simulation of thermocapillary convection with deformable free surface using boundary-fitted coordinates. Numer. Heat Transfer B 32, 127–149.

Anaturk, A.R., Szeri, A.Z., 1992. Stability of flow between infinite rotating disks. J. Math. Phys. Sci. 26, 569–581.

Batchelor, G.K., 1951. Note on a class of solutions of the Navier–Stokes equations representing steady rotationally symmetric flow. Quart. J. Mech. Applied Math. 4, 29–41.

Canuto, C., Hussaini, M.Y., Quateroni, A., Zang, T. A., 1988. Spectral Methods in Fluid Dynamics, Springer, New York.

Chang, C.J., Humphrey, J.A.C., Grief, R., 1990. Calculation of turbulent convection between corotating disks in axisymmetric enclosures. Int. J. Heat Mass Transfer 33, 2701–2720.

Chang, C.J., Schuler, C.A., Humphrey, J.A.C., Grief, R., 1989. Flow and heat transfer between two corotating disks in an axisymmetric enclosure. J. Heat Transfer 111, 625–632.

Chin, D.T., Litt, M., 1972. An electrochemical study of flow instability on a rotating disk. J. Fluid Mech. 54, 613–625.

Ehrenstein, U., Peyret, R.A., 1989. Chebyshev-collocation method for the Navier-Stokes equations with application to double-diffusive convection. Int. J. Numer. Methods Fluids 9, 427–452.

Elena, L., Schiestel, R., 1995. Turbulence modeling of confined flow in rotating disk systems. AIAA J. 33, 813–821.

Gan, X., Kilic, M., Owen, J.M., 1994. Superposed flow between two discs contrarotating at differential speeds. Int. J. Heat and Fluid Flow 15, 438–446.

Haidvogel, D.B., Zang, T.A., 1979. The accurate solution of Poisson's equation by expansion in Chebyshev polynomials. J. Comp. Phys. 30, 167–180.

Hill, R.W., Ball, K.S., 1997. Chebyshev collocation analysis of axisymmetric flow and heat transfer between counter-rotating disks. J. Fluids Eng. 119, 940–947.

Hill, R.W., 1998. Parallel Implementation of a Fourier–Chebyshev Spectral Method for the Three-dimensional Navier–Stokes Equations and Application to Transitional Flow in Cylindrical Geometries. Ph.D. Dissertation, The University of Texas at Austin.

Hill, R.W., Ball, K.S., 1999. Parallel implementation of a Fourier–Chebyshev collocation method for the incompressible Navier–Stokes equations. Numer. Heat Transfer, in press.

Holodniok, M., Kubicek, M., Hlavacek, V., 1977. Computation of the flow between two rotating coaxial disks. J. Fluid Mech. 81, 689–699.

Holodniok, M., Kubicek, M., Hlavacek, V., 1981. Computation of the flow between two rotating coaxial disks: Multiplicity of steady-state solutions. J. Fluid Mech. 108, 227–240.

Humphrey, J.A.C., Chang, C.J., Schuler, C.A., 1991. Unobstructed and obstructed rotating disk flows: A summary review relevant to information storage systems. Advances Information Storage Systems 1, 79–110.

Humphrey, J.A.C., Schuler, C.A., Webster, D.R., 1995. Unsteady laminar flow between a pair of disks corotating in a fixed cylindrical enclosure. Phys. Fluids A 7, 1225–1240.

Iacovides, H., Chew, J.W., 1993. The computation of convective heat transfer in rotating cavities. Int. J. Heat and Fluid Flow 14, 146–154.

Iglesias, I., Humphrey, J.A.C., 1998. Two- and three-dimensional laminar flows between disks corotating in a fixed cylindrical enclosure. Int. J. Numer. Methods Fluids 26, 581–603.

Kilic, M., Gan, X., Owen, J.M., 1994. Transitional flow between contra-rotating disks. J. Fluid Mech. 281, 119–135.

Kleiser, L., Schumann, U., 1980. Treatment of incompressibility and boundary conditions in 3-D numerical spectral simulations of plane channel flows. In: Proceedings of the Third GAMM Conference on Numer. Methods Fluid Mech., Vieweg, Braunschweig, pp. 165–173.

Kobayashi, R., 1994. Review: Laminar to turbulent transition of three-dimensional boundary layers on rotating bodies. J. Fluids Eng. 116, 200–211.

Ku, H.C., Hirsh, R.S., Taylor, T.D., 1987. A pseudospectral method for solution of the three-dimensional incompressible Navier–Stokes equations. J. Comp. Phys. 70, 439–462.

Kuo, D.C., Ball, K.S., 1997. Taylor–Couette flow with buoyancy: Onset of spiral flow. Phys. Fluids 9, 2872–2884.

Lai, C.Y., Rajagopal, K.R., Szeri, A.Z., 1984. Asymmetric flow between parallel rotating disks. J. Fluid Mech. 146, 203–225.

LeQuéré, P., Pécheux, J., 1989. Numerical simulations of multiple flow transitions in axisymmetric annulus convection. J. Fluid Mech. 206, 517–544.

Madabhushi, R.K., Balachandar, S., Vanka, S.P., 1993. A divergence-free Chebyshev collocation procedure for incompressible flows with two non-periodic directions. J. Comp. Phys. 105, 199–206.

Nesreddine, H., Nguyen, C.T., Vo-Ngoc, D., 1995. Laminar flow between a stationary and a rotating disk with radial throughflow. Numer. Heat Transfer A 27, 537–557.

Patera, A.T., Orszag, S.A., 1982. Instability of pipe flow. Non-linear Problems: Present and Future, North-Holland, Amsterdam, pp. 367–377.

Radel, V.S., Szeri, A.Z., 1997. Symmetry breaking bifurcation in finite disk flow. Phys. Fluids 9, 1650–1656.

Randriamampianina, A., Elena, L., Fountaine, J.P., Schiestel, R., 1997. Numerical prediction of laminar, transitional and turbulent flows in shrouded rotor–stator systems. Phys. Fluids 9, 1696–1713.

Schuler, C.A., Usry, W., Wever, B., Humphrey, J.A.C., Grief, R., 1990. On the flow in the unobstructed space between shrouded corotating disks. Phys. Fluids A 2, 1760–1770.

Stewartson, K., 1953. On the flow between two rotating coaxial disks. Proc. Cambridge Philos. Soc. 49, 333–341.

Szeri, A.Z., Adams, M.L., 1978. Laminar throughflow between closely spaced rotating disks. J. Fluid Mech. 86, 1–14.

Szeri, A.Z., Schneider, S.J., Labbe, F., Kaufman, H.N., 1983a. Flow between rotating disks. Part 1. Basic flow. J. Fluid Mech. 134, 103–131.

Szeri, A.Z., Giron, A., Schneider, S.J., Kaufman, H.N., 1983b. Flow between rotating disks. Part 2. Stability. J. Fluid Mech. 134, 133–154.

Tuckerman, L.S., 1989. Divergence-free velocity fields in non-periodic geometries. J. Comp. Phys. 80, 403–441.

von Karman, Th., 1921. Über laminare und turbulente reibung. Z. Angew. Math. Mech. 1, 233–252.

Wahal, S., Oztekin, A., Bornside, D.E., Brown, R.A., Seidel, P.K., Ackmann, P.W., Geyling, F.T., 1993. Visualization of a gas flow instability in spin coating systems. Applied Phys. Lett. 62, 2584–2586.

Yang, H.H., Shizgal, B., 1994. Chebyshev pseudospectral multi-domain technique for viscous flow calculation. Comput. Methods Applied Mech. Eng. 118, 47–61.

Zang, T.A., 1991. On the rotation and skew-symmetric forms for incompressible flow simulations. Applied Numer. Math. 7, 27–40.